HDGS: Textured 2D Gaussian Splatting for Enhanced Scene Rendering

Yunzhou Song[1*]   Heguang Lin[1*]   Jiahui Lei[1†]   Lingjie Liu[1]   Kostas Daniilidis[1,2]

[1]University of Pennsylvania   [2]Archimedes, Athena RC

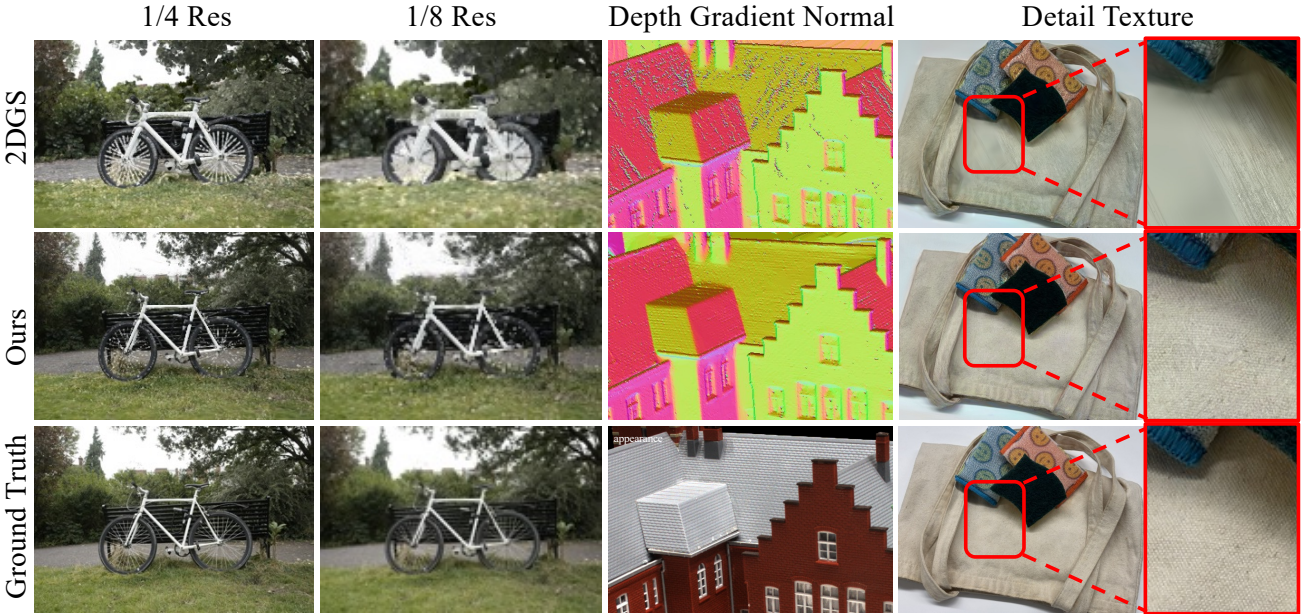{timsong, hglin, leijh, lingjie.liu, kostas}@upenn.edu

Figure 1. Overview of the improvements in our method over 2D Gaussian Splatting (2DGS). *First two columns*: Our frustum-based sampling technique effectively mitigates aliasing for high-frequency appearance rendering at reduced resolutions (1/4 and 1/8). *Third column*: Our approach yields enhanced geometric consistency with smoother surface normals. *Last column*: Our method disentangles geometry from appearance by utilizing a per-Gaussian texture map, allowing for rich detail preservation that 2DGS cannot resolve.

Abstract

Recent advancements in neural rendering, particularly 2D Gaussian Splatting (2DGS), have shown promising results for jointly reconstructing fine appearance and geometry by leveraging 2D Gaussian surfels. However, current methods face significant challenges when rendering at arbitrary viewpoints, such as anti-aliasing for down-sampled rendering, and texture detail preservation for high-resolution rendering. We proposed a novel method to align the 2D surfels with texture maps and augment it with per-ray depth sorting and fisher-based pruning for rendering consistency and efficiency. With correct order, per-surfel texture maps significantly improve the capabilities to capture fine details. Additionally, to render high-fidelity details in varying viewpoints, we designed a frustum-based sampling method to mitigate the aliasing artifacts. Experimental results on benchmarks and our custom texture-rich dataset demonstrate that our method surpasses existing techniques, particularly in detail preservation and anti-aliasing.

1. Introduction

Neural rendering has made remarkable strides in novel view synthesis and geometry reconstruction. Recently, 2D Gaussian Splatting (2DGS) [14] emerged as a promising method that leverages Gaussian surfels to represent complex scenes. Despite its advantages, however, the current 2DGS technique encounters the challenge of rendering high-quality images from arbitrary resolution and distance. Close-up rendering often suffers from insufficient detail, whereas aliasing artifacts arise when rendering at low resolutions

---

*equal contribution, † corresponding author

1

or from distant viewpoints. These flaws hinder the realism and quality of 3D rendering by compromising visual fidelity at varying resolutions and distances. This paper explores solutions to high-definition 3D scene reconstruction using 2D Gaussian Splatting, enabling visualization from arbitrary viewpoints and resolutions.

Gaussian Splatting struggles when appearance details exceed geometric resolution in close views. The entanglement of geometry and appearance in Gaussian Splatting requires numerous primitives for accurate representation. We proposed a novel method to assign each primitive with an optimizable texture map to disentangle the appearance with geometry. However, the straightforward implementation suffers from significant generalization issues and popping artifacts from novel views. We identify that the artifacts stem from 2DGS's global per-view primitive sorting, which we address by switching to per-ray sorting [29] as regularization. Additionally, since assigning a per-surfel texture map introduces higher memory demand, we apply Fisher-information-based pruning [11] to remove Gaussians with high uncertainty to maintain an efficient representation.

On the other hand, the aliasing artifact has been an emerging issue in Gaussian Splatting when rendering from arbitrary viewpoints. Previous works [40, 42] proposed multiple filters to address this issue. However, adapting these techniques to 2DGS is non-trivial, as the projection of the 2D surfels onto the image plane is no longer Gaussian distributed. To address this issue in 2DGS, we propose a frustum-based sampling technique. By treating each pixel as a light frustum that samples over a volume, rather than a single ray from its center, our approach reduces aliasing artifacts in high-frequency regions and provides smoother rendering across varying resolutions.

Equipped with per-surfel texture maps, as well as per-ray sorting and pruning, our system can efficiently render high-quality images from close-up viewpoints. Augmented with a frustum-based sampling strategy, our pipeline significantly mitigates aliasing artifacts from distant viewpoints, resulting in an alias-free method to render high-quality images from arbitrary viewpoints. Our contributions are summarized as:

- We proposed HDGS, a 2DGS-based method with per-surfel texture maps that can be rendered correctly with per-ray sorting and maintain efficiency through Fisher-information-based pruning.
- We introduced a frustum-based Gaussian sampling method to mitigate high-frequency rendering aliases.
- Our pipeline achieves state-of-the-art rendering quality on standard benchmarks. We collected a texture-rich dataset, on which our method can capture fine details that other baseline methods fail to preserve.

2. Related Work

Anti-aliasing in novel view synthesis. Following the pioneering neural radiance field (NeRF) [25], numerous works [1, 2, 13] have introduced novel methods for anti-aliasing in neural rendering. Zip-NeRF [3] presented a multi-sampling strategy to enable anti-aliasing within a more efficient hash code-based representation [26] for neural radiance fields. Recently, Rip-NeRF [22] proposed a Ripmap-encoded Platonic solid representation for anti-aliased neural radiance fields. With the emergence of 3D Gaussian Splatting [19] and its extensions in material modeling [18, 32], avatar creation [28, 43], and dynamic scene reconstruction [39], novel approaches have been developed to address aliasing in 3D Gaussian Splatting. For example, [20, 34] applied scale-adaptive modifications during optimization, which can be used as a plugin in any pretrained 3D Gaussian splatting. [40, 42] analyze the approximated Gaussian primitive covariance after the affine projection and add post-process filters to suppress the high-frequency signals in 3D Gaussian Splatting. However, the 2D Gaussian Splatting adopts precise projection for each primitive onto the image plane, which is no longer Gaussian distributed. Therefore, we proposed a frustum-based sampling strategy to increase the sampling frequency to mitigate the anti-aliasing issues in 2DGS.

Texturing 3D representations. 3D representations can have different forms of parametrization, such as neural networks [25, 33, 37], voxel grid [10, 27, 36], and a hybrid of feature grids and networks [6, 23, 24]. Follow-up works texture these representations by optimizing a surface parametrization [8, 35], while other works disentangle appearance and geometry with combined methods [15, 41]. The most relevant two works have attempted to disentangle geometry and appearance by introducing texture maps in Gaussian Splatting [30, 38]. The approach in [38] applies the texture map with the assumption that Gaussians in the scene lie on a surface topologically similar to a sphere. Such an assumption failed in the scenes with complicated geometry. In [30], the surfel nature of 2DGS is leveraged to train a per-Gaussian texture map after geometry reconstruction. However, this approach substantially increases computational demands, leading to failure on complicated scenes and not addressing aliasing artifacts.

Popping Artifact of Rasterization Gaussian Splatting rasterizer sorts the center depth of all primitives once for each view and traverses them by the same global order along the ray. As a result, for the same 3D area the blending order of primitives may differ from training views and test views, which introduces the popping artifact. Methods including [4, 5, 29, 31] tried to approximately per-ray sort the primitives with limited resources and computing. While some other techniques design order-free blending methods like [12].
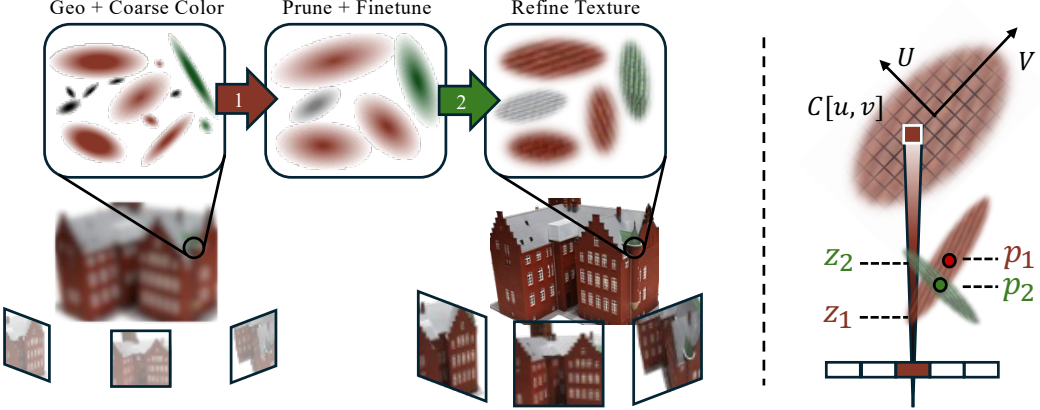
Figure 2. Our proposed method for high-quality scene reconstruction leverages the explicit per-ray depth and 2D ray-surfel intersection coordinates of 2D Gaussian Splatting. The left image illustrates our coarse-to-fine pipeline, which begins with 2DGS training, proceeds through Fisher pruning, and ends with per-surfel texture mapping for enhanced visual fidelity. The right image highlights our design of per-ray sorting strategy with primitive texture: though the center of surfel p_2 is closer to the screen than p_1, our method sorts the Gaussians correctly as z_1 and z_2 in the depth order.

3. Method

3.1. Preliminaries

2D Gaussian Splatting. Huang at al. [14] proposed to represent 3D scenes with 2D Gaussian surfels to reconstruct the appearance and fine-level geometry jointly. Each Gaussian surfel is parameterized with two principal tangential axis vectors $\mathbf{t_u}$ and $\mathbf{t_v}$ paired with two scaling factors s_u and s_v, the surfel center $\mathbf{p}$, opacity α, and the spherical harmonics parameters $\mathbf{c}$. The surfel normal $\mathbf{n}$ is then defined by $\pm(\mathbf{t_u} \times \mathbf{t_v})$, where the direction is towards the viewing direction.

Given a pixel $\mathbf{x}$ in the image space, instead of projecting the primitive center to the image plane and approximating the projected covariance as the 3DGS does, the 2D Gaussian Splatting computes the explicit precise ray-surfel intersection (u, v) in the surfel coordinates by the projection matrix $\mathbf{P}$ and the splat-to-world transformation $\mathbf{H}$ as

$$\mathbf{x} = (xz, yz, z, z)^\top = \mathbf{PH}(u, v, 1, 1)^\top, \quad (1)$$

the transformation $\mathbf{H}$ is defined by the surfel parameters as

$$\mathbf{H} = \begin{bmatrix} s_u\mathbf{t_u} & s_v\mathbf{t_v} & 0 & \mathbf{p} \\ 0 & 0 & 0 & 1 \end{bmatrix} \quad (2)$$

Then the surfel weight is computed by querying a normalized Gaussian distribution as $G(\mathbf{x}) = \exp(-\frac{u^2+v^2}{2})$. The pixel color $\mathbf{C}$, depth D, and surface normal $\mathbf{N}$ are then accumulated across all intersected surfels along the ray from front to back by alpha-blending:

$$\mathbf{C}(\mathbf{x}) = \sum_i \mathbf{c}_i(\mathbf{d})\alpha_i G_i(\mathbf{x})T_i \quad (3)$$

$$D(\mathbf{x}) = \sum_i z_i(\mathbf{x})\alpha_i G_i(\mathbf{x})T_i \quad (4)$$

$$\mathbf{N}(\mathbf{x}) = \sum_i \mathbf{n}_i\alpha_i G_i(\mathbf{x})T_i \quad (5)$$

where $T_i = \prod_j^{i-1}(1 - \alpha_j G_j)$ is the transmittance, and $\mathbf{d}$ is the viewing direction. During optimization, the 2DGS introduces two geometric regularizations Eq.6, Eq.7 to capture fine-grained surfaces, where $\mathbf{N}_d$ is the normal map computed by the gradient of the depth map.

$$L_d = \sum_{i,j} \alpha_i G_i T_i \alpha_j G_j T_j (z_i - z_j)^2 \quad (6)$$

$$L_n = \sum_i \alpha_i G_i T_i (1 - \mathbf{n}_i \mathbf{N}_d) \quad (7)$$

Fisher Information for 3D Gaussian Pruning. Prior works have explored various approaches to compress 3D Gaussian-based scene representations, such as uncertainty quantification [11, 17], and hybrid method [9]. Fisher information provides a principled way to quantify the uncertainty in parameter estimates. In 3D scene reconstruction, this uncertainty arises from the inherently underconstrained nature of projecting 3D scenes onto 2D images. Gaussians not well-constrained by multiple camera views may be able to reconstruct the input views from a range of locations and scales. To quantify this uncertainty mathematically, we start with the L_2 error over the input reconstruction images $\mathbf{I}_G$:

$$L_2 = \frac{1}{2} \sum_{\phi \in P_{gt}} ||\mathbf{I}_\mathcal{G}(\phi) - \mathbf{I}_{gt}||_2^2 \quad (8)$$

The Hessian of this loss function captures the sensitivity of the error to changes in Gaussian parameters:

$$\nabla_\mathcal{G}^2 L_2 = \sum_{\phi \in P_{gt}} \nabla_\mathcal{G}\mathbf{I}_\mathcal{G}(\phi)\nabla_\mathcal{G}\mathbf{I}_\mathcal{G}(\phi)^T$$
$$+ (\mathbf{I}_\mathcal{G}(\phi) - \mathbf{I}_{gt})\nabla_\mathcal{G}^2\mathbf{I}_\mathcal{G}(\phi) \quad (9)$$

3

$G_{avg} \uparrow$ $G_{avg} \downarrow$

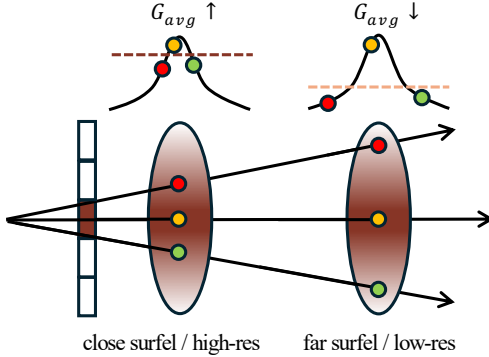close surfel / high-res   far surfel / low-res

Figure 3. **Frustum Sampling.** The average density of the sampled primitive decreases as the surfel moves farther from the camera or as the sampling resolution decreases, effectively acting as a low-pass filter for anti-aliasing.

For a converged model where the reconstruction error approaches zero, the second term vanishes, leaving us with the Fisher approximation:

$$\nabla_{\mathcal{G}}^2 L_2 = \sum_{\phi \in P_{gt}} \nabla_{\mathcal{G}} \mathbf{I}_{\mathcal{G}} \nabla_{\mathcal{G}} \mathbf{I}_{\mathcal{G}}^T \qquad (10)$$

This approximation depends only on the input poses P_{gt} and not the input images I_{gt}. We can then compute a per-Gaussian sensitivity score by taking the block Hessian for each Gaussian's parameters. Gaussians with lower sensitivity scores are candidates for pruning as they have less impact on the reconstruction error.

3.2. Frustum-based Sampling

To model and render the high-frequency appearance details in diverse views and resolutions, we can not avoid tackling the anti-aliasing issues. The aliasing effect may occur when sampling a continuous signal by a discrete function especially when the sampling frequency is less than twice the signal frequency, known as the Nyquist Theorem. In the field of computer graphics and rendering, the sampling frequency is determined by the image's pixel resolution, while the signal frequency is related to the object's appearance complexity after projection to the image plane. Due to the feature of perspective projection, objects far from the camera with low appearance complexity may be crowded into small areas on the image plane, which leads to higher appearance frequency and may trigger aliasing.

Recent 3D Gaussian Splatting anti-aliasing techniques [40, 42] analyze the approximated Gaussian primitive co-variance after the affine projection and add post-process filters to suppress the high-frequency signals. However, the 2D Gaussian Splatting adopts precise projection for each primitive, whose projection is no longer Gaussian distributed. As the post-process methods become non-trivial in the 2D Gaussian Splatting setting, we consider increasing the sampling rate to mitigate the aliasing effect by estimating the average Gaussian density. Each pixel on the sensor

receives exactly the light of a frustum, rather than only one ray shooting out from the center. For each 2D pixel of size $(2\delta_x, 2\delta_y)$ sampling a surfel in 3D space, we then cast the center ray $\mathbf{x}$ and four corner rays to compute 5 intersections, and average the sampled Gaussian density as Eq. 11 for the following alpha-blending.

$$\hat{G}(\mathbf{x}) = w_m G(\mathbf{x}) + \sum_{i,j \in \{1,-1\}} w_c G(\mathbf{x} + (i\delta_y, j\delta_x)) \quad (11)$$

We are not casting 5 individual subpixel rays for each pixel, which causes 5 times more computing, but compute the intersections of the frustum with the same surfel touched by the center ray. Please refer to supplementary materials for comparison with different sampling weights w_m, w_c. Illustrated in Fig. 3, as the frustum diverges along distance, the high-frequency primitives in the distance will have a smaller weight, which equals low-pass filtering for anti-aliasing. Meanwhile, lower sampling resolution leads to a larger frustum diameter, which also suppresses the high-frequency details. Our method precisely and efficiently captures the high-frequency signals as the ray-surfel intersection is closed and has a low computing cost.

3.3. Per-Ray Sorting with Fisher Pruning

The Gaussian splatting rasterization sorts the primitives by their center depths per view before rendering and then traverses them in the same order for different pixel rays during alpha blending. As a result, popping artifacts occur due to the primitives' order difference of the same 3D position in different views, which hinders the novel view rendering fidelity. This phenomenon is more obvious when rendering high-frequency details or incorporating thin and large primitives. We leverage the explicit depth z of 2D Gaussian Splatting to implement the per-ray k-buffer sorting [4] and per-tile sorting in [29]. We set the tile size as 8 and compute the center pixel depth of the tile to leverage the per-tile radix sorting. We set the ray sort buffer size k as 24 for synthetic scenes and 16 for real scenes for efficiency.

While ray sorting significantly mitigates popping artifacts, it introduces computational overhead and can impact convergence due to increased ordering complexity between adjacent rays. Therefore, it becomes beneficial to reduce the number of surfels while preserving the scene's visual quality. To address these challenges, we introduce a Fisher information-based pruning strategy inspired by [11] for our 2D surfel representation.

Given a 2D Gaussian surfel G_i, we compute its sensitivity score using a block-wise Fisher information matrix similar to equation 10. As suggested in [11], we only consider the spatial position x_i and scaling s_i parameters when computing the Jacobian, as they are most relevant to the geometric uncertainty. Then We compute the sensitivity score
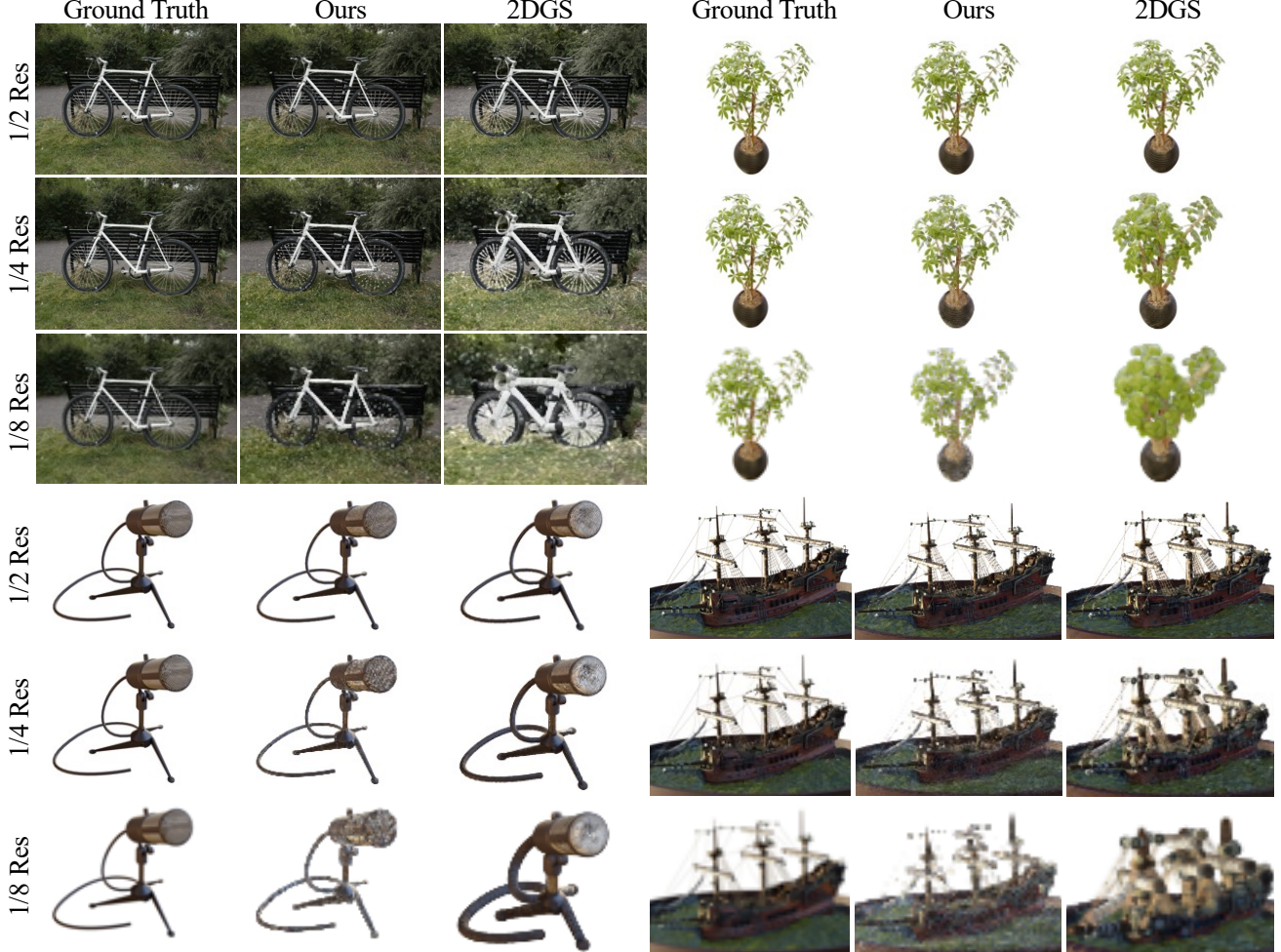
4

Figure 4. Comparison of our method and 2DGS at reduced resolutions (1/2, 1/4, 1/8) on NeRF synthetic dataset [25] and Mip-NeRF 360 dataset [2]. Our approach effectively mitigates dilation artifacts and aliasing problems in 2DGS. Note that the 1/8 rendering of the microphone by 2DGS has the same image scale as above, whose dilation aliasing is considerably severe.

	PSNR ↑					SSIM ↑					LPIPS ↓				
	Full Res.	1/2 Res.	1/4 Res.	1/8 Res.	Avg.	Full Res.	1/2 Res.	1/4 Res.	1/8 Res.	Avg.	Full Res.	1/2 Res.	1/4 Res.	1/8 Res	Avg.
NeRF [25]	31.48	32.43	30.29	26.70	30.23	0.949	0.962	0.964	0.951	0.956	0.061	0.041	0.044	0.067	0.053
MipNeRF [2]	**33.08**	**33.31**	**30.91**	**27.97**	**31.31**	**0.961**	**0.970**	**0.969**	**0.961**	**0.965**	**0.045**	**0.031**	**0.036**	**0.052**	**0.041**
3DGS [19]	33.33	26.95	21.38	17.69	24.84	0.969	0.949	0.875	0.766	0.890	**0.030**	0.032	0.066	0.121	0.063
MipSplatting [42]	**33.36**	**34.00**	**31.85**	**28.67**	**31.97**	0.969	**0.977**	**0.978**	**0.973**	**0.974**	0.031	**0.019**	**0.019**	**0.026**	**0.024**
2DGS [14]	32.67	27.19	20.57	16.65	24.27	0.967	0.949	0.851	0.717	0.871	0.035	0.038	0.085	0.155	0.078
Ours	**33.46**	32.16	28.18	23.98	29.45	0.968	0.969	0.951	0.913	0.950	**0.030**	0.027	0.049	0.088	0.049

Table 1. Reduced resolution rendering on the NeRF synthetic dataset [25]. All methods are trained on full-resolution images and evaluated at four lower resolutions to simulate zoom-out effects. Our method consistently outperforms 2DGS across different resolutions.

U_i for each surfel as the L_1-norm of the log of the diagonal elements of its Fisher information matrix:

$$U_i = || \log(\text{diag}(\sum_{\phi \in P_{gt}} \nabla_{x_i, s_i} \mathbf{I}_{\mathcal{G}_i} \nabla_{x_i, s_i} \mathbf{I}_{\mathcal{G}_i}^T))||_1 \quad (12)$$

This process enables us to identify less impactful surfels while maintaining rendering quality and view consistency through the ray sorting mechanism.

3.4. Per-Surfel Texture

The per-ray sorting strategy functions as a regularization to stabilize the multi-view rendering consistency, which increases pressure in the appearance fitting performance as studied by [29]. Meanwhile, the adaptive control procedures in Gaussian optimization prunes low opacity primitives which tend to model the high-frequency details. We assign an optimizable texture map, rather than a single RGB color to each surfel at the second stage to overcome this

5

drawback. The benefit of texture maps can be explained in two domains: 1) Adding more optimizable parameters to balance the performance drop introduced by the per-ray depth sorting regularization. 2) Enabling each surfel to model a more complex and detailed appearance.

Given a surfel with scaling factors (s_u, s_v), we assign it with a texture map $\mathbf{C}[u,v]$ of size (U, V, c), $U = \lceil Ts_u \rceil$, $V = \lceil Ts_v \rceil$, where c is the number of color channels, and T is a hyperparameter determined by the memory and number of primitives empirically. A texture resolution upper bound is set to constraint memory consumption and all textures are initialized by the background color. During rendering, we only use the center ray for each pixel frustum to query the texture map. For each ray-surfel intersection with surfel coordinates (u, v) we set a cutoff range r as 4.5 and compute the indexing coordinate as $(\frac{u+r}{2r}U, \frac{v+r}{2r}V)$ to bilinearly sample the texture map to get the 0-th component of the Spherical Harmonics. Different from [14, 19, 30], we compute the view direction of the surfel as the precise camera-intersection direction $\mathbf{d} = \mathbf{H}(u, v, 1)^\top - \mathbf{O}$, rather than the approximated camera-center direction $\mathbf{p} - \mathbf{O}$ considering large surfels, where $\mathbf{O}$ is the camera center in world coordinates. Now the per-pixel alpha blending equation is formulated as Eq.14, where the index i follows the k-sorted order, and $\mathbf{SH}$ is the spherical parameter rendering.

$$\hat{\mathbf{C}}(\mathbf{x}) = \mathbf{C}[u, v] + \mathbf{SH}(\mathbf{d}) \tag{13}$$

$$\mathbf{C}(\mathbf{x}) = \sum_i \hat{\mathbf{C}}(\mathbf{x})_i \alpha_i \hat{G}_i(\mathbf{x}) T_i \tag{14}$$

3.5. Optimization

Our method contains 2 optimization stages as shown in Fig. 2: 1) Train a representation whose primitives have only a single color with Fisher pruning. 2) Assign each surfel with texture, and finetune the representation with on-demand higher-resolution images. We follow the 2D Gaussian Splatting for the training target

$$L = L_c + \lambda_n L_n + \lambda_d L_d \tag{15}$$

where L_c is the appearance reconstruction loss which sums the L_1 loss and the SSIM loss, and L_n, L_d are geometric regularization as Eq.6,7. During the second stage, we stop the gradient of Gaussian centers, rotations, and scales, as the high-frequency rendering responds to geometry modification significantly.

4. Experiments

4.1. Evaluation Setup

We evaluate our pipeline through comparisons of both appearance and geometry against state-of-the-art methods. We choose the Mip-NeRF 360 [2] dataset and the NeRF synthetic [25] dataset for appearance comparison, and DTU dataset [16] for geometry comparison. Additionally, we

Method	Mip-NeRF 360 [2]			NeRF synthetic [25]		
	PSNR ↑	SSIM↑	LPIPS ↓	PSNR ↑	SSIM↑	LPIPS ↓
3DGS [19]	27.24	0.815	0.214	33.33	0.969	0.030
StopPop [29]	27.27	0.814	0.213	**33.57**	**0.970**	0.030
PGSR [7]	27.43	**0.830**	0.193	31.87	0.964	0.035
MipSplatting[42]	**27.73**	0.828	**0.189**	33.36	0.969	0.031
2DGS [14]	27.03	0.805	0.223	32.67	0.967	0.035
GSTex [30]	-	-	-	33.25	**0.969**	**0.024**
Ours	**27.25**	**0.807**	**0.216**	**33.46**	0.968	0.030

Table 2. Mean quantitative results on Mip-NeRF 360 [2] and NeRF sythetic [25] dataset.

Method	PSNR ↑	SSIM↑	LPIPS ↓	$\|HF\|$ ↑
3DGS [19]	22.40	0.602	0.461	0.304
2DGS [14]	22.11	**0.627**	0.460	0.342
Ours	**22.72**	0.607	**0.350**	**0.434**

Table 3. Quantitative results on our texture-rich dataset.

order err ϵ	Train	Test
2DGS [14]	0.2392	0.2713
Ours w/o prune	0.0023	0.0024
Ours w/ prune	0.0021	0.0021

Method	CD
2DGS [14]	0.74
Ours	0.75

Table 4. The train and test views average sorting error after k-sorting of the NeRF synthetic dataset.

Table 5. The Chamfer distance measured on the DTU [16] dataset.

present results on a self-captured, texture-rich dataset. Unless stated otherwise, we prune 10% of the surfels after the original 2DGS training. We set the sampling weights w_m and w_c as 0.2, and the texture resolution T as 1000 for the NeRF synthetic dataset, 400 for Mip-NeRF 360 indoor scenes, 200 for outdoor scenes, and 4000 for our texture-rich dataset. We compare our method with 3DGS-based methods like StopPop [29], PGSR [7], and 2DGS-based methods like GSTex [30]. We evaluate the PSNR, SSIM, and L-PIPS for novel view rendering, and measure the Chamfer distance for geometric reconstruction. We conduct all the experiments on a single NVIDIA L40 GPU.

4.2. Experiment Result

Quantitative comparison. Tab. 5 illustrates that our method sustains a geometric reconstruction quality comparable to the baseline on the DTU dataset [16]. For appearance reconstruction, we evaluate our approach on the Mip-NeRF 360 [2] dataset and the NeRF synthetic dataset [25], with results presented in Tab. 2. Our method achieves superior appearance metrics compared to 2DGS while remaining competitive with methods emphasizing appearance over geometry, such as 3DGS [19] and StopThePop [29]. Our method reaches a mean primitive number of 1.3×10^5 on the NeRF synthetic dataset and 2.6×10^6 on the Mip-NeRF 360 dataset, compared with 2DGS which has 1.4×10^5 and 2.2×10^6 and MipSplatting which has 3.0×10^5 and 4.2×10^6 respectively.

To further analyze the high-frequency texture expressiv-

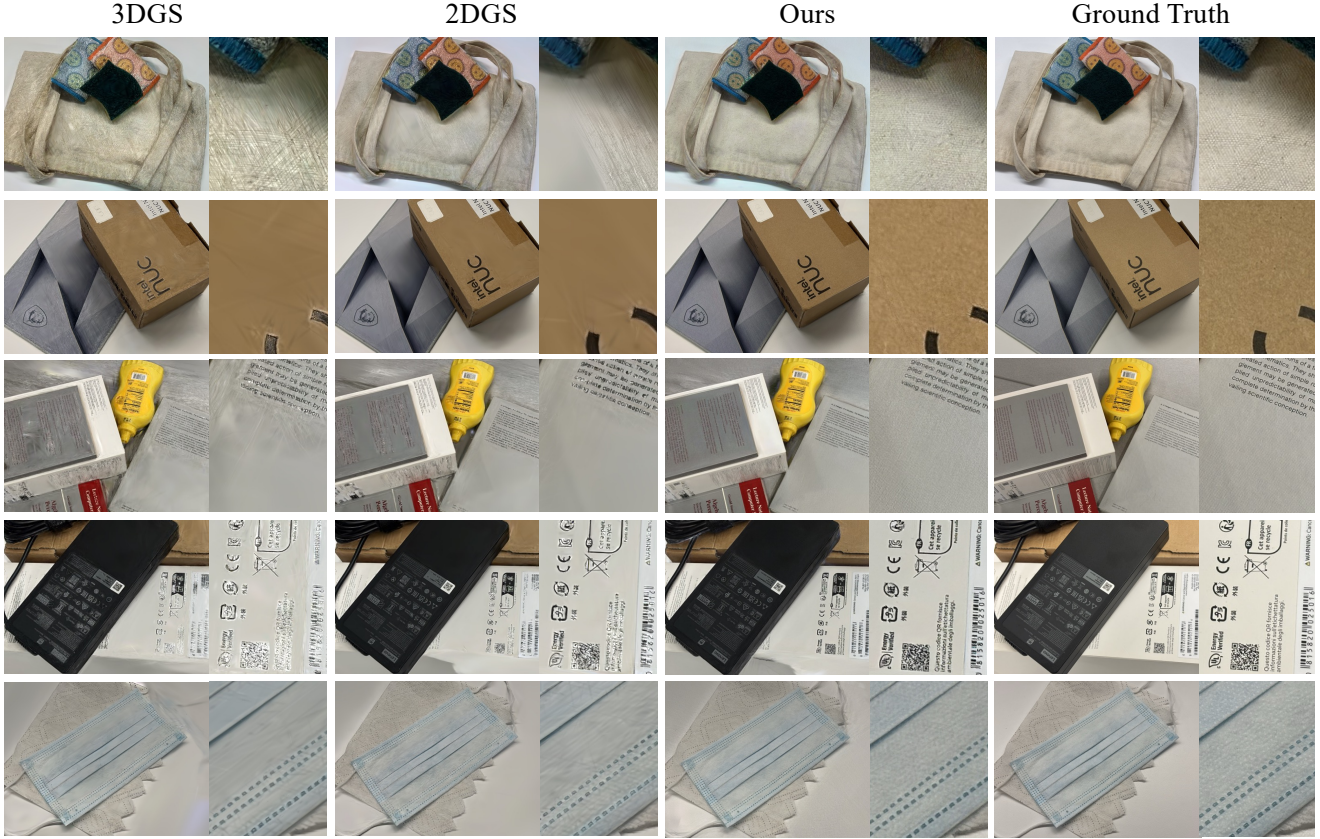| 3DGS	2DGS	Ours	Ground Truth

Figure 5. Quanlitative comparison of novel view rendering on five custom scenes featuring materials with intricate details of our method with 3D Gaussian Splatting (3DGS) and 2D Gaussian Splatting (2DGS). Each row showcases a distinct texture-rich material novel view rendering: 1) the fabric texture on a bag, 2) the paper surface of a cardboard box, 3) the text and texture of the book cover, 4) the label details on a box, 5) fine texture of a face mask. The four columns display results from 3DGS, 2DGS, our method, and the ground truth. Across all scenes, our approach consistently captures finer details, demonstrating superior texture fidelity compared to 3DGS and 2DGS.
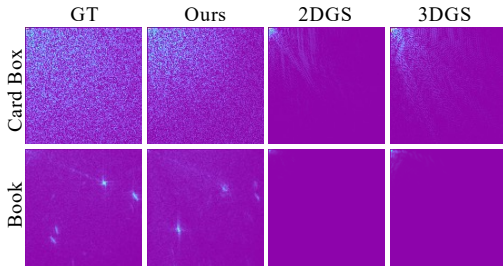

Figure 6. Visualization of DCT on the texture-rich area of our customized dataset. Right-top represents low-frequency, right-bottom represents low-frequency. Our method preserves more high-frequency details than baselines.

$$||HF|| = \frac{DCT_{AC}(\hat{\mathbf{I}}) \cdot DCT_{AC}(\mathbf{I})}{||DCT_{AC}(\hat{\mathbf{I}})||_2 ||DCT_{AC}(\mathbf{I})||_2} \quad (16)$$

Qualitative Comparison. Fig. 4 illustrates the rendering quality at reduced resolutions (1/2, 1/4 and 1/8), where our method significantly reduces the aliasing artifacts commonly observed in 2DGS. We show the result on the NeRF synthetic dataset as the scene includes rich details on the surface. Tab. 7 presents a comparison of novel view surface normals computed from depth gradients between our method and 2DGS, demonstrating that our approach achieves smoother surfaces and enhances geometric consistency. Fig. 5 showcases various texture-rich scenes from our custom dataset, including the fabric of a bag, a cardboard texture, a detailed book cover, a labeled box, and the fine texture of a face mask. For these challenging materials, our method consistently outperforms both 3DGS and 2DGS, effectively preserving high-frequency details. The DCT result of the cardboard box and the book is shown in Fig. 6, highlighting that our method retains more high-frequency details than the competing methods.

ity of our method, we apply the Discrete Cosine Transform (DCT) to texture-rich regions of both rendered and ground truth images. By measuring the cosine distance of the non-constant components, we quantify high-frequency fidelity as defined in Eq.16, where $\hat{\mathbf{I}}$ denotes the rendered image and $\mathbf{I}$ is the ground truth image. The results shown in Tab. 3 indicate our method preserves more high-frequency details than 2DGS and 3DGS.

Figure 7. Surface normal comparison between our method, 2DGS, and ground truth appearance in **novel views** on DTU [16] dataset. We split the test and training set as [21]. Our approach achieves smoother surfaces and enhances geometric consistency relative to 2DGS.
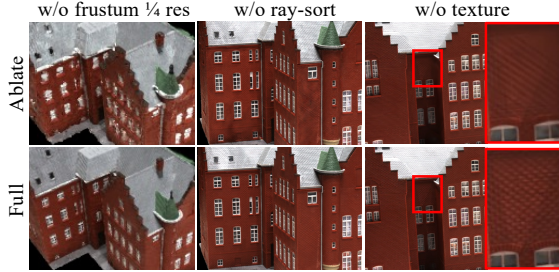

Figure 8. Qualitative ablation study. We show the qualitative result on the test views of scan24 in the DTU dataset [16] when removing frustum-based sampling, texture, and ray sorting, respectively.

Method	PSNR ↑	SSIM ↑	LPIPS ↓
full	33.46	0.968	0.030
w/o texture	33.28	0.968	0.032
w/o prune	33.40	0.967	0.031
w/o sorting	31.99	0.955	0.048
w/o frustum	33.27	0.967	0.031

Table 6. Ablation study on NeRF synthetic [25] dataset.

4.3. Ablation Study

We conduct an ablation study to evaluate the impact of key design choices on appearance reconstruction using the NeRF synthetic dataset [25]. We examine four crucial components: texture maps, Fisher-based pruning, ray sorting, and frustum-based anti-aliasing. Tab. 6 presents the quantitative results when removing each component. Fig. 8 shows the qualitative results when removing frustum-based sampling, texture, and ray sorting. We analyze the impact of removing each one of the components:

Texture Maps: Removing texture maps results in decreased PSNR and increased LPIPS, with particularly noticeable degradation in scenes containing fine details. This validates our hypothesis that per-primitive texture maps enable better modeling of high-frequency appearance details.

Fisher information-based Pruning: [29] introduces an approach to calculating the sorting error of a rendering. For each ray, it computes a per-ray depth order error ϵ as:

$$\epsilon = \sum_i (z_i - z_{i+1}) \cdot \mathbb{1}[z_{i+1} < z_i] \qquad (17)$$

where z_i is the blending depth of the i-th surfel along the ray, and $\mathbb{1}[\cdot]$ is the indicator function when consecutive surfels are out of order. The error is averaged over all the rays on one image. Our analysis demonstrates that incorporating Fisher information pruning reduces the sorting order error for both training and testing datasets, as shown in Tab. 4.

Ray Sorting: Ray sorting proves crucial for our approach, as its removal causes the most significant drop across all metrics, as the popping artifacts become particularly severe when the scene is overfitted by per-surfel texture without sorting.

Frustum-based Sampling: While removing the frustum-based sampling strategy only slightly impacts the metrics, we find this design particularly valuable for low-resolution and distant view rendering as shown in Fig. 8.

5. Conclusions

In conclusion, our proposed pipeline achieves high-fidelity scene rendering by addressing limitations in detailed texture preservation and anti-aliasing that have challenged previous Gaussian splatting approaches. Through frustum-based sampling, Fisher-based pruning, per-ray sorting, and per-surfel texture mapping, our technique achieves robust performance across benchmark datasets and our texture-rich scenes.

Limitation. Despite the strong performance of our method in preserving fine details and reducing artifacts,

the computational cost of our per-ray sorting and texture map indexing remains higher than baseline methods, which could impact scalability in real-time applications or on devices with limited GPU resources.

References

[1] Jonathan T Barron, Ben Mildenhall, Matthew Tancik, Peter Hedman, Ricardo Martin-Brualla, and Pratul P Srinivasan. Mip-nerf: A multiscale representation for anti-aliasing neural radiance fields. In *Proceedings of the IEEE/CVF international conference on computer vision*, pages 5855–5864, 2021. 2

[2] Jonathan T Barron, Ben Mildenhall, Dor Verbin, Pratul P Srinivasan, and Peter Hedman. Mip-nerf 360: Unbounded anti-aliased neural radiance fields. In *Proceedings of the IEEE/CVF conference on computer vision and pattern recognition*, pages 5470–5479, 2022. 2, 5, 6, 1, 3

[3] Jonathan T Barron, Ben Mildenhall, Dor Verbin, Pratul P Srinivasan, and Peter Hedman. Zip-nerf: Anti-aliased grid-based neural radiance fields. In *Proceedings of the IEEE/CVF International Conference on Computer Vision*, pages 19697–19705, 2023. 2

[4] Louis Bavoil, Steven P. Callahan, Aaron Lefohn, João L. D. Comba, and Cláudio T. Silva. Multi-fragment effects on the gpu using the k-buffer. In *Proceedings of the 2007 Symposium on Interactive 3D Graphics and Games*, page 97–104, New York, NY, USA, 2007. Association for Computing Machinery. 2, 4

[5] Steven P. Callahan, Milan Ikits, Joao L. D. Comba, and Claudio T. Silva. Hardware-assisted visibility sorting for unstructured volume rendering. *IEEE Transactions on Visualization and Computer Graphics*, 11(3):285–295, 2005. 2

[6] Anpei Chen, Zexiang Xu, Andreas Geiger, Jingyi Yu, and Hao Su. Tensorf: Tensorial radiance fields. In *European conference on computer vision*, pages 333–350. Springer, 2022. 2

[7] Danpeng Chen, Hai Li, Weicai Ye, Yifan Wang, Weijian Xie, Shangjin Zhai, Nan Wang, Haomin Liu, Hujun Bao, and Guofeng Zhang. Pgsr: Planar-based gaussian splatting for efficient and high-fidelity surface reconstruction. *arXiv preprint arXiv:2406.06521*, 2024. 6, 4

[8] Sagnik Das, Ke Ma, Zhixin Shu, and Dimitris Samaras. Learning an isometric surface parameterization for texture unwrapping. In *European Conference on Computer Vision*, pages 580–597. Springer, 2022. 2

[9] Zhiwen Fan, Kevin Wang, Kairun Wen, Zehao Zhu, Dejia Xu, and Zhangyang Wang. Lightgaussian: Unbounded 3d gaussian compression with 15x reduction and 200+ fps. *arXiv preprint arXiv:2311.17245*, 2023. 3

[10] Sara Fridovich-Keil, Alex Yu, Matthew Tancik, Qinhong Chen, Benjamin Recht, and Angjoo Kanazawa. Plenoxels: Radiance fields without neural networks. In *Proceedings of the IEEE/CVF conference on computer vision and pattern recognition*, pages 5501–5510, 2022. 2

[11] Alex Hanson, Allen Tu, Vasu Singla, Mayuka Jayawardhana, Matthias Zwicker, and Tom Goldstein. Pup 3d-gs: Principled uncertainty pruning for 3d gaussian splatting. *arXiv preprint arXiv:2406.10219*, 2024. 2, 3, 4

[12] Qiqi Hou, Randall Rauwendaal, Zifeng Li, Hoang Le, Farzad Farhadzadeh, Fatih Porikli, Alexei Bourd, and Amir Said. Sort-free gaussian splatting via weighted sum rendering, 2024. 2

[13] Wenbo Hu, Yuling Wang, Lin Ma, Bangbang Yang, Lin Gao, Xiao Liu, and Yuewen Ma. Tri-miprf: Tri-mip representation for efficient anti-aliasing neural radiance fields. In *Proceedings of the IEEE/CVF International Conference on Computer Vision*, pages 19774–19783, 2023. 2

[14] Binbin Huang, Zehao Yu, Anpei Chen, Andreas Geiger, and Shenghua Gao. 2d gaussian splatting for geometrically accurate radiance fields. In *SIGGRAPH 2024 Conference Papers*. Association for Computing Machinery, 2024. 1, 3, 5, 6, 4

[15] Yi-Hua Huang, Yan-Pei Cao, Yu-Kun Lai, Ying Shan, and Lin Gao. Nerf-texture: Texture synthesis with neural radiance fields. In *ACM SIGGRAPH 2023 Conference Proceedings*, pages 1–10, 2023. 2

[16] Rasmus Jensen, Anders Dahl, George Vogiatzis, Engin Tola, and Henrik Aanæs. Large scale multi-view stereopsis evaluation. In *Proceedings of the IEEE conference on computer vision and pattern recognition*, pages 406–413, 2014. 6, 8, 1, 3

[17] Wen Jiang, Boshu Lei, and Kostas Daniilidis. Fisherrf: Active view selection and uncertainty quantification for radiance fields using fisher information. *arXiv preprint arXiv:2311.17874*, 2023. 3

[18] Yingwenqi Jiang, Jiadong Tu, Yuan Liu, Xifeng Gao, Xiaoxiao Long, Wenping Wang, and Yuexin Ma. Gaussianshader: 3d gaussian splatting with shading functions for reflective surfaces. In *Proceedings of the IEEE/CVF Conference on Computer Vision and Pattern Recognition*, pages 5322–5332, 2024. 2

[19] Bernhard Kerbl, Georgios Kopanas, Thomas Leimkühler, and George Drettakis. 3d gaussian splatting for real-time radiance field rendering. *ACM Transactions on Graphics*, 42 (4), 2023. 2, 5, 6, 1, 3, 4

[20] Jiameng Li, Yue Shi, Jiezhang Cao, Bingbing Ni, Wenjun Zhang, Kai Zhang, and Luc Van Gool. Mipmap-gs: Let gaussians deform with scale-specific mipmap for anti-aliasing rendering, 2024. 2

[21] Zhaoshuo Li, Thomas Müller, Alex Evans, Russell H Taylor, Mathias Unberath, Ming-Yu Liu, and Chen-Hsuan Lin. Neuralangelo: High-fidelity neural surface reconstruction. In *IEEE Conference on Computer Vision and Pattern Recognition (CVPR)*, 2023. 8

[22] Junchen Liu, Wenbo Hu, Zhuo Yang, Jianteng Chen, Guoliang Wang, Xiaoxue Chen, Yantong Cai, Huan-ang Gao, and Hao Zhao. Rip-nerf: Anti-aliasing radiance fields with ripmap-encoded platonic solids. In *ACM SIGGRAPH 2024 Conference Papers*, pages 1–11, 2024. 2

[23] Lingjie Liu, Jiatao Gu, Kyaw Zaw Lin, Tat-Seng Chua, and Christian Theobalt. Neural sparse voxel fields. *Advances in Neural Information Processing Systems*, 33:15651–15663, 2020. 2

[24] Stephen Lombardi, Tomas Simon, Gabriel Schwartz, Michael Zollhoefer, Yaser Sheikh, and Jason Saragih. Mixture of volumetric primitives for efficient neural rendering. *ACM Transactions on Graphics (ToG)*, 40(4):1–13, 2021. 2

[25] Ben Mildenhall, Pratul P. Srinivasan, Matthew Tancik, Jonathan T. Barron, Ravi Ramamoorthi, and Ren Ng. Nerf: Representing scenes as neural radiance fields for view synthesis. In *ECCV*, 2020. 2, 5, 6, 8, 1, 3, 4

[26] Thomas Müller, Alex Evans, Christoph Schied, and Alexander Keller. Instant neural graphics primitives with a multiresolution hash encoding. *ACM transactions on graphics (TOG)*, 41(4):1–15, 2022. 2

[27] Richard A Newcombe, Shahram Izadi, Otmar Hilliges, David Molyneaux, David Kim, Andrew J Davison, Pushmeet Kohi, Jamie Shotton, Steve Hodges, and Andrew Fitzgibbon. Kinectfusion: Real-time dense surface mapping and tracking. In *2011 10th IEEE international symposium on mixed and augmented reality*, pages 127–136. Ieee, 2011. 2

[28] Shenhan Qian, Tobias Kirschstein, Liam Schoneveld, Davide Davoli, Simon Giebenhain, and Matthias Nießner. Gaussianavatars: Photorealistic head avatars with rigged 3d gaussians. In *Proceedings of the IEEE/CVF Conference on Computer Vision and Pattern Recognition*, pages 20299–20309, 2024. 2

[29] Lukas Radl, Michael Steiner, Mathias Parger, Alexander Weinrauch, Bernhard Kerbl, and Markus Steinberger. StopThePop: Sorted Gaussian Splatting for View-Consistent Real-time Rendering. *ACM Transactions on Graphics*, 4 (43), 2024. 2, 4, 5, 6, 8, 3

[30] Victor Rong, Jingxiang Chen, Sherwin Bahmani, Kiriakos N Kutulakos, and David B Lindell. Gstex: Per-primitive texturing of 2d gaussian splatting for decoupled appearance and geometry modeling. *arXiv preprint arXiv:2409.12954*, 2024. 2, 6, 4

[31] Marco Salvi and Karthik Vaidyanathan. Multi-layer alpha blending. In *Proceedings of the 18th Meeting of the ACM SIGGRAPH Symposium on Interactive 3D Graphics and Games*, page 151–158, New York, NY, USA, 2014. Association for Computing Machinery. 2

[32] Yahao Shi, Yanmin Wu, Chenming Wu, Xing Liu, Chen Zhao, Haocheng Feng, Jingtuo Liu, Liangjun Zhang, Jian Zhang, Bin Zhou, et al. Gir: 3d gaussian inverse rendering for relightable scene factorization. *arXiv preprint arXiv:2312.05133*, 2023. 2

[33] Vincent Sitzmann, Julien Martel, Alexander Bergman, David Lindell, and Gordon Wetzstein. Implicit neural representations with periodic activation functions. *Advances in neural information processing systems*, 33:7462–7473, 2020. 2

[34] Xiaowei Song, Jv Zheng, Shiran Yuan, Huan-ang Gao, Jingwei Zhao, Xiang He, Weihao Gu, and Hao Zhao. Sags: Scale-adaptive gaussian splatting for training-free anti-aliasing. *arXiv preprint arXiv:2403.19615*, 2024. 2

[35] Pratul P Srinivasan, Stephan J Garbin, Dor Verbin, Jonathan T Barron, and Ben Mildenhall. Nuvo: Neural uv mapping for unruly 3d representations. In *European Conference on Computer Vision*, pages 18–34. Springer, 2025. 2

[36] Cheng Sun, Min Sun, and Hwann-Tzong Chen. Direct voxel grid optimization: Super-fast convergence for radiance fields reconstruction. In *Proceedings of the IEEE/CVF conference on computer vision and pattern recognition*, pages 5459–5469, 2022. 2

[37] Matthew Tancik, Pratul Srinivasan, Ben Mildenhall, Sara Fridovich-Keil, Nithin Raghavan, Utkarsh Singhal, Ravi Ramamoorthi, Jonathan Barron, and Ren Ng. Fourier features let networks learn high frequency functions in low dimensional domains. *Advances in neural information processing systems*, 33:7537–7547, 2020. 2

[38] Tian-Xing Xu, Wenbo Hu, Yu-Kun Lai, Ying Shan, and Song-Hai Zhang. Texture-gs: Disentangling the geometry and texture for 3d gaussian splatting editing. In *European Conference on Computer Vision*, pages 37–53. Springer, 2025. 2

[39] Yunzhi Yan, Haotong Lin, Chenxu Zhou, Weijie Wang, Haiyang Sun, Kun Zhan, Xianpeng Lang, Xiaowei Zhou, and Sida Peng. Street gaussians for modeling dynamic urban scenes. *arXiv preprint arXiv:2401.01339*, 2024. 2

[40] Zhiwen Yan, Weng Fei Low, Yu Chen, and Gim Hee Lee. Multi-scale 3d gaussian splatting for anti-aliased rendering. In *Proceedings of the IEEE/CVF Conference on Computer Vision and Pattern Recognition*, pages 20923–20931, 2024. 2, 4

[41] Bangbang Yang, Chong Bao, Junyi Zeng, Hujun Bao, Yinda Zhang, Zhaopeng Cui, and Guofeng Zhang. Neumesh: Learning disentangled neural mesh-based implicit field for geometry and texture editing. In *European Conference on Computer Vision*, pages 597–614. Springer, 2022. 2

[42] Zehao Yu, Anpei Chen, Binbin Huang, Torsten Sattler, and Andreas Geiger. Mip-splatting: Alias-free 3d gaussian splatting. In *Proceedings of the IEEE/CVF Conference on Computer Vision and Pattern Recognition*, pages 19447–19456, 2024. 2, 4, 5, 6, 3

[43] Wojciech Zielonka, Timur Bagautdinov, Shunsuke Saito, Michael Zollhöfer, Justus Thies, and Javier Romero. Drivable 3d gaussian avatars. *arXiv preprint arXiv:2311.08581*, 2023. 2

HDGS: Textured 2D Gaussian Splatting for Enhanced Scene Rendering

Supplementary Material

Method	PSNR ↑	SSIM↑	LPIPS ↓	$\|\|HF\|\|$ ↑
3DGS [19]	22.40	0.602	0.461	0.304
2DGS [14]	22.11	**0.627**	0.460	0.342
Ours	**22.72**	0.607	**0.350**	**0.434**
Ours w/o texture	22.58	0.624	0.455	0.345

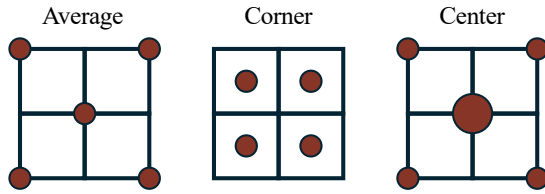Table 7. Quantitative results on our texture-rich dataset.

Figure 9. Visualization of different sampling strategy

6. Further ablation

We present a comprehensive ablation study in Tab. 13 to evaluate the impact of key design choices on appearance reconstruction. Additionally, we report results from another ablation study conducted on our customized texture-rich dataset, examining the effect of removing per-surfel texture in Tab. 7. The influence of different pruning percentages is analyzed in Tab. 8.

7. Sampling Strategy Error Analysis

There are multiple alternative sampling strategies to numerically approximate the average density, e.g. the integral value of the intersection of the pixel frustum and the 2D Gaussian surfel. Given the sampling points in a pixel P, e.g. $(x_i, y_i) \in [-0.5, 0.5]^2$, we can determine the parameters w_i to approximate the integrated value by the polynomials of the sampled function value on sampling points as Eq. 18.

$$\iint_P f(x,y)dxdy = \sum_i w_i f(x_i, y_i) + O((x+y)^n) \quad (18)$$

Through the Taylor Series, we have the estimated integral function value f in a small region $P = h \times h$ around the origin $(0,0)$ as Eq. 19.

$$\int_{-h/2}^{h/2}\int_{-h/2}^{h/2} f(x,y)dxdy$$
$$= \iint_P \left(f(0,0) + f'_x(0,0)x + f'_y(0,0)y + O((x+y)^2) \right) dxdy$$
$$= h^2 f(0,0) + \frac{h^4 f''_{xx}(0,0)}{24} + \frac{h^4 f''_{yy}(0,0)}{24} + O(h^6) \quad (19)$$

As the function value at $(x_i, y_i) \in \{\pm h/2, \pm h/2\}$ can be written as the approximation of the Taylor Expansion at $(0,0)$, we can analyze and cancel the higher order errors by the linear combination of sampled values. For 4 corner points, we have

$$\frac{h^2}{4}\left(f(\frac{-h}{2},\frac{-h}{2}) + f(\frac{h}{2},\frac{-h}{2}) + f(\frac{-h}{2},\frac{h}{2}) + f(\frac{h}{2},\frac{h}{2}) \right)$$
$$= h^2 f(0,0) + \frac{h^4 f''_{xx}(0,0)}{8} + \frac{h^4 f''_{yy}(0,0)}{8} + O(h^6)$$
$$= \iint_P f(x,y)dxdy + \frac{h^4 f''_{xx}(0,0)}{12} + \frac{h^4 f''_{yy}(0,0)}{12} + O(h^6)$$
$$= \iint_P f(x,y)dxdy + O(h^4) \quad (20)$$

This means all the w_i equals $\frac{1}{4}$ in Eq. 18 as illustrated in Fig. 9 the Corner case. To further cancel the 4-th order error, we can involve the function value at $(0,0)$. The error term of $f(0,0)$ can be written as

$$h^2 f(0,0) = \iint_P f(x,y)dxdy - \frac{h^4 f''_{xx}(0,0)}{24} - \frac{h^4 f''_{yy}(0,0)}{24}$$
$$+ O(h^6) \quad (21)$$

So we can cancel the $o(h^4)$ error item by

$$\frac{h^2}{12}\left(8f(0,0) + \sum_{i,j \in \{-1,1\}} f(i\frac{h}{2}, j\frac{h}{2}) \right) \quad (22)$$
$$= \iint_P f(x,y)dxdy + O(h^6)$$

This means the weights in Eq. 18 are $\frac{1}{12}$ and $\frac{2}{3}$ for the four corner points and the center point respectively, as illustrated in Fig. 9 the Center case. However, the theoretical error may not always hold in real scenarios, where the vanilla average of 5 points used in the main paper may be more robust. We report the rendering quality of different strategies in different resolutions in Tab. 9 and show the qualitative results on selected scenes in Fig. 10. The strategy we adopt in the main paper performs best on the full resolution, while other methods have better results on some other resolutions. As a result, different strategies can be adopted for various tasks.

8. Full results

We show the full comparison of our models versus previous works on the DTU dataset [16], Mip-NeRF 360 [2] dataset and the NeRF synthetic dataset [25] in Tab. 11,Tab. 10, Tab. 12, respectively.
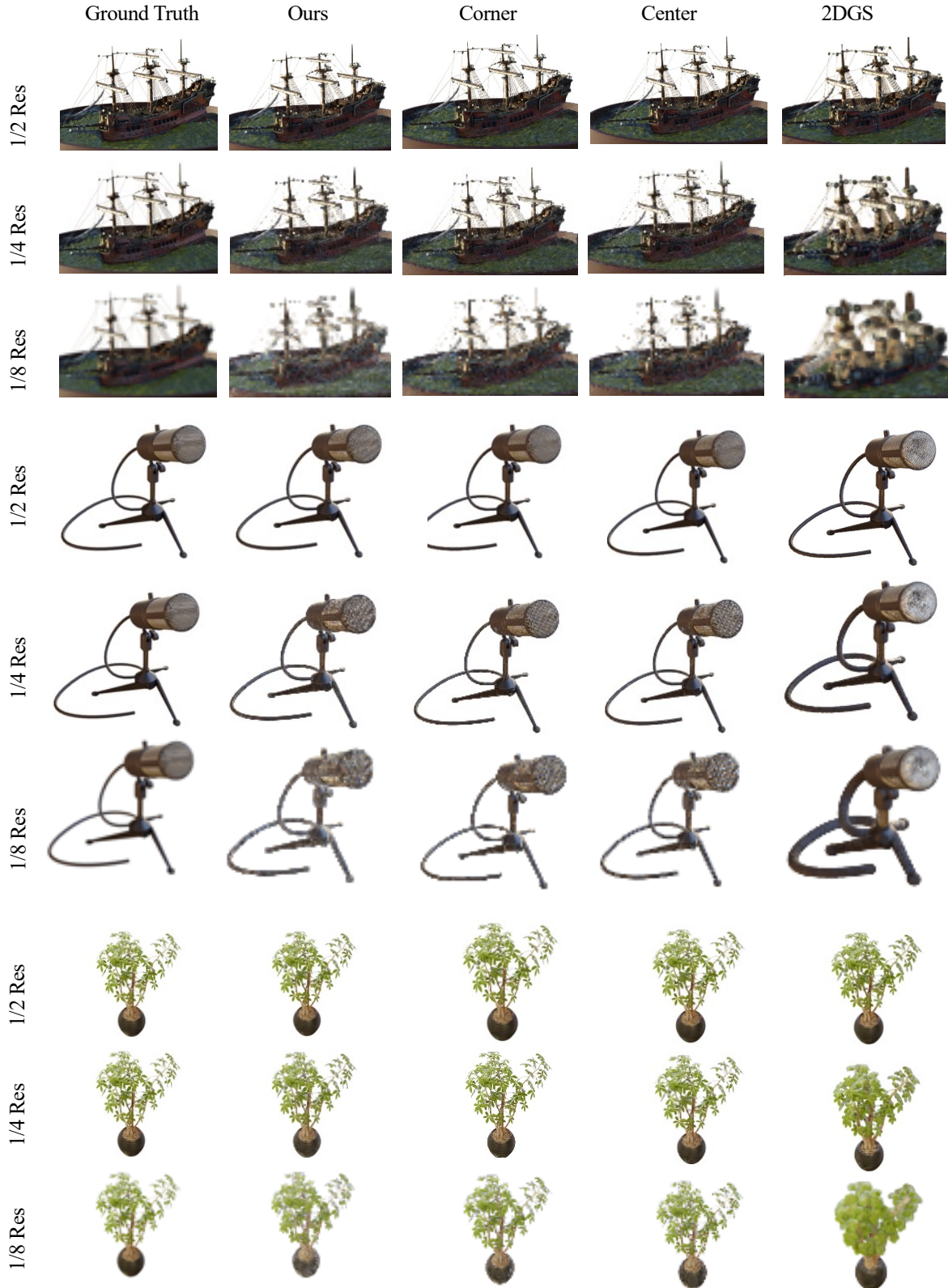
Figure 10. Reduced resolution rendering on the NeRF synthetic dataset [25] for different sampling strategy: Ours(average), Corner(Eq. 20), Center(Eq. 22). All methods are trained on full-resolution images and evaluated at four lower resolutions to simulate zoom-out effects.

Pruned %	chair	drums	ficus	hotdog	lego	materials	mic	ship	mean
10% (Ours)	35.92	26.05	35.90	38.08	35.37	29.87	35.36	31.10	**33.46**
20%	35.90	26.06	35.91	38.04	35.31	29.85	35.33	31.09	33.44
30%	35.89	26.05	35.83	38.02	35.39	29.83	35.37	31.12	33.44
40%	35.83	26.00	35.80	37.84	35.34	29.71	35.36	31.14	33.38
50%	35.69	25.87	35.73	37.52	35.16	29.45	35.34	31.19	33.24
10% (Ours)	0.986	0.952	0.988	0.986	0.981	0.957	0.991	0.901	**0.968**
20%	0.986	0.952	0.988	0.986	0.981	0.957	0.991	0.901	0.968
30%	0.986	0.953	0.988	0.986	0.981	0.956	0.991	0.902	0.968
40%	0.986	0.952	0.988	0.986	0.980	0.954	0.991	0.902	0.967
50%	0.985	0.951	0.988	0.986	0.979	0.951	0.991	0.903	0.967
10% (Ours)	0.013	0.042	0.011	0.019	0.017	0.037	0.007	0.094	**0.030**
20%	0.013	0.042	0.011	0.019	0.017	0.037	0.007	0.094	0.030
30%	0.013	0.042	0.011	0.018	0.017	0.038	0.007	0.094	0.030
40%	0.014	0.043	0.011	0.018	0.018	0.040	0.007	0.095	0.031
50%	0.015	0.045	0.012	0.019	0.019	0.043	0.007	0.096	0.032

Table 8. Pruning ablation on NeRF synthetic dataset [25], We report PSNR ↑, SSIM ↑, LPIPS ↓ respectively.

	PSNR ↑					SSIM ↑					LPIPS ↓				
	Full Res.	1/2 Res.	1/4 Res.	1/8 Res.	Avg.	Full Res.	1/2 Res.	1/4 Res.	1/8 Res.	Avg.	Full Res.	1/2 Res.	1/4 Res.	1/8 Res	Avg.
3DGS [19]	33.33	26.95	21.38	17.69	24.84	0.969	0.949	0.875	0.766	0.890	**0.030**	0.032	0.066	0.121	0.063
MipSplatting [42]	**33.36**	**34.00**	**31.85**	**28.67**	**31.97**	0.969	**0.977**	**0.978**	**0.973**	**0.974**	0.031	**0.019**	**0.019**	**0.026**	**0.024**
2DGS [14]	32.67	27.19	20.57	16.65	24.27	0.967	0.949	0.851	0.717	0.871	0.035	0.038	0.085	0.155	0.078
Ours	**33.46**	32.16	28.18	23.98	29.45	**0.968**	0.969	0.951	0.913	0.950	**0.030**	0.027	0.049	0.088	0.049
Ours Center Eq. 22	33.26	33.29	**30.49**	**26.77**	**30.95**	0.967	0.972	0.964	0.943	0.962	0.030	**0.024**	**0.039**	**0.073**	**0.042**
Ours Corner Eq. 20	33.35	**33.35**	30.45	26.61	30.94	0.967	**0.973**	**0.966**	**0.944**	**0.963**	0.030	0.025	0.042	0.075	0.043

Table 9. Reduced resolution rendering on the NeRF synthetic dataset [25]. All methods are trained on full-resolution images and evaluated at four lower resolutions to simulate zoom-out effects. Our method consistently outperforms 2DGS across different resolutions.

	bicycle	flowers	garden	stump	treehill	room	counter	kitchen	bonsai	mean
Ours	24.83	21.22	26.98	26.40	22.50	31.20	28.94	31.09	32.06	27.25
2DGS [14]	24.82	20.99	26.91	26.41	22.52	30.86	28.45	30.62	31.64	27.03
3DGS [19]	24.71	21.09	26.63	26.45	22.33	31.50	29.07	31.13	32.26	27.24
StopPop [29]	25.20	21.50	27.16	26.69	22.43	30.83	28.59	31.13	31.93	**27.27**
Ours	0.742	0.588	0.857	0.760	0.608	0.925	0.909	0.928	0.943	0.807
2DGS [14]	0.752	0.588	0.852	0.765	0.627	0.912	0.900	0.919	0.933	0.805
3DGS [19]	0.771	0.605	0.868	0.775	0.638	0.914	0.905	0.922	0.938	**0.815**
StopPop	0.767	0.604	0.862	0.775	0.635	0.917	0.903	0.925	0.939	0.814
Ours	0.231	0.340	0.115	0.223	0.354	0.201	0.188	0.119	0.177	0.216
2DGS [14]	0.218	0.346	0.115	0.222	0.329	0.223	0.208	0.133	0.214	0.223
3DGS [19]	0.205	0.336	0.103	0.210	0.317	0.220	0.204	0.129	0.205	0.214
StopPop [29]	0.206	0.335	0.107	0.210	0.319	0.216	0.200	0.126	0.202	**0.213**

Table 10. Quantitative results on Mip-NeRF 360 [2] dataset. We report PSNR ↑, SSIM ↑, LPIPS ↓, respectively.

Scene	24	37	40	55	63	65	69	83	97	105	106	110	114	118	122	Mean
Ours	0.45	0.80	0.33	0.37	0.89	0.91	0.76	1.32	1.23	0.67	0.64	1.19	0.38	0.71	0.56	0.75
2DGS [14]	0.46	0.80	0.33	0.37	0.95	0.86	0.80	1.25	1.24	0.67	0.67	1.24	0.39	0.64	0.47	**0.74**

Table 11. Quantitative result on the DTU Dataset [16] on Chamfer distance ↓.

Method	chair	drums	ficus	hotdog	lego	materials	mic	ship	mean
3DGS [19]	35.90	26.16	34.85	37.70	35.78	30.00	35.42	30.90	33.34
StopPop [29]	35.70	26.23	35.58	37.93	36.30	30.50	36.53	31.77	**33.57**
PGSR [7]	34.90	25.83	31.99	35.92	33.74	28.80	34.17	29.64	31.87
GSTex [30]	35.51	26.06	35.65	37.49	35.51	29.72	35.28	30.80	33.25
2DGS	34.24	26.10	35.40	36.97	34.03	29.54	34.64	30.46	32.67
Ours	35.92	26.05	35.90	38.08	35.37	29.87	35.36	31.10	33.46
3DGS [19]	0.987	0.955	0.987	0.985	0.983	0.960	0.992	0.907	0.969
StopPop [29]	0.988	0.955	0.987	0.986	0.983	0.961	0.992	0.906	0.970
PGSR [7]	0.985	0.951	0.978	0.984	0.978	0.954	0.990	0.890	0.964
2DGS [14]	0.984	0.954	0.988	0.984	0.978	0.957	0.990	0.904	0.967
GSTex [30]	0.987	0.954	0.988	0.985	0.982	0.958	0.991	0.904	**0.969**
Ours	0.986	0.952	0.988	0.986	0.981	0.957	0.991	0.901	0.968
3DGS [19]	0.012	0.037	0.012	0.020	0.016	0.034	0.006	0.107	0.030
StopPop [29]	0.010	0.036	0.012	0.019	0.016	0.036	0.006	0.104	0.030
PGSR [7]	0.015	0.039	0.020	0.022	0.020	0.042	0.008	0.116	0.035
2DGS [14]	0.017	0.040	0.012	0.024	0.023	0.039	0.008	0.114	0.035
GSTex [30]	0.009	0.038	0.008	0.013	0.011	0.020	0.006	0.085	0.024
Ours	0.013	0.042	0.011	0.019	0.017	0.037	0.007	0.094	**0.030**

Table 12. Quantitative result on NeRF synthetic dataset [25], We report PSNR ↑, SSIM ↑, LPIPS ↓ respectively.

Method	chair	drums	ficus	hotdog	lego	materials	mic	ship	mean
Ours	35.92	26.05	35.90	38.08	35.37	29.87	35.36	31.10	**33.46**
w/o texture	35.59	26.04	35.81	37.74	35.25	29.86	35.24	30.73	33.28
w/o pruning	35.80	26.06	35.96	37.95	35.30	29.82	35.32	31.02	33.40
w/o sorting	34.16	25.63	35.12	35.76	33.23	29.05	33.34	29.64	31.99
w/o frustum	35.66	26.06	35.89	37.23	34.99	29.75	35.43	31.19	33.27
Ours	0.986	0.952	0.988	0.986	0.981	0.957	0.991	0.901	**0.968**
w/o texture	0.985	0.953	0.988	0.985	0.980	0.958	0.991	0.904	0.968
w/o pruning	0.986	0.952	0.989	0.985	0.980	0.956	0.991	0.900	0.967
w/o sorting	0.978	0.942	0.985	0.973	0.965	0.941	0.980	0.872	0.955
w/o frustum	0.986	0.954	0.989	0.985	0.979	0.956	0.991	0.902	0.967
Ours	0.013	0.042	0.011	0.019	0.017	0.037	0.007	0.094	**0.030**
w/o texture	0.015	0.041	0.011	0.022	0.019	0.036	0.007	0.103	0.032
w/o pruning	0.014	0.042	0.011	0.019	0.018	0.038	0.008	0.095	0.031
w/o sorting	0.023	0.055	0.016	0.046	0.036	0.061	0.027	0.122	0.048
w/o frustum	0.015	0.040	0.011	0.020	0.020	0.038	0.008	0.095	0.031

Table 13. Ablation study on NeRF synthetic dataset [25], We report PSNR ↑, SSIM ↑, LPIPS ↓ respectively.